AALBORG UNIVERSITY

DENMARK

Modeling and Operation of Series-Parallel Resonant Load in Industrial RF Dielectric Heating Application

Ahmad, Faheem; Jørgensen, Asger Bjørn; Munk-Nielsen, Stig

Modeling and Operation of Series-Parallel Resonant Load in Industrial RF Dielectric Heating Application

Faheem Ahmad ⓘ, Asger Bjørn Jørgensen ⓘ, and Stig Munk-Nielsen ⓘ, *Member, IEEE*

Abstract—**Radio Frequency (RF) based heating application is used in multiple industries like drying cross-laminated woods, food and packaging, melting silicon etc. These industrial RF heating plants operate at frequencies of 6.78 MHz, 13.56 MHz, or 27.12 MHz (ISM band). Historically, the high frequency requirement has forced the industry to rely on vacuum tube based RF generator, which are only 60% efficient. Modern semiconductors like wide bandgap (WBG) devices have achieved the high frequency operation that is required to replace the inefficient vacuum tubes. However, a comprehensive study of load network for an industrial RF heating plant has not been undertaken such that an existing plant can be retrofitted with semiconductor based turn-key solution. In this paper the authors present design equations for an industrial RF dielectric heating load structure and suggest necessary modifications required to replace vacuum tube RF generator with voltage source converter (VSC). A new figure of merit (FOM) is defined that impacts the load structure efficiency. Finally, a small-scale prototype load is manufactured as a case study. The prototype demonstrated an output power of 750 W at 6.76 MHz with an overall efficiency of 90% from DC input to RF load which can not be achieved with a vacuum tube technology.**

Index Terms—**Compensation, dielectric heating, induction heating, semiconductor devices, wood industry.**

I. INTRODUCTION

ABOUT 20% of total energy consumption across the globe is used for industrial heating applications such as drying wood pulp and laminated wood, melting metals, food and packaging [1]. In the United States more than 50% of its industrial direct greenhouse gas (GHG) emissions is due to burning fossil fuel in aforementioned applications. Thus, there is an opportunity to reduce human carbon footprint by electrification of such industrial processes. Electric industrial heating can be categorized into two main methodologies - induction and dielectric [2]. Induction heating is applied in the frequency range of few 100 kHz - 3 MHz while dielectric heating mostly operates from 5-30 MHz [3], [4]. Both these methodologies together can be referred to as radio frequency (RF) heating. Induction heating occurs when the work material is placed inside an electromagnetic field. This induces high circulating current in the work material which generates heat. Therefore induction heating is only used for heating metallic materials

such as heating of steel, metal hardening or zone melting of silicon for producing ultra-pure silicon for the semiconductor industry. On the other hand dielectric heating applies an alternating electric field to heat up non-metallic work materials such as cooking and packaging of food products, textile and paper manufacturing or drying glued cross-laminated wood that can be used in civil infrastructure as an alternative for cement [5]–[7].

Industrial RF heating plants require RF generators. Historically the high voltage, high frequency required by the RF generators can only be generated by vacuum tubes. Fig. 1(a) shows a schematic of push-pull type RF generator circuit using vacuum tube for dielectric heating [2]. The schematic comprises of a grid voltage step-up transformer which is then rectified to high voltage (HV) DC. The HV DC is then fed to oscillator tubes which outputs RF power to a resonant tank circuit including the load. In this example the work material is directly coupled to the RF generator. Fig. 1(b) shows examples of indirectly coupled load structures of induction and dielectric heating [8].

In the past 50 years several industries have transformed by incorporating semiconductor devices, such as power generation and distribution. Past decade has seen exponential growth
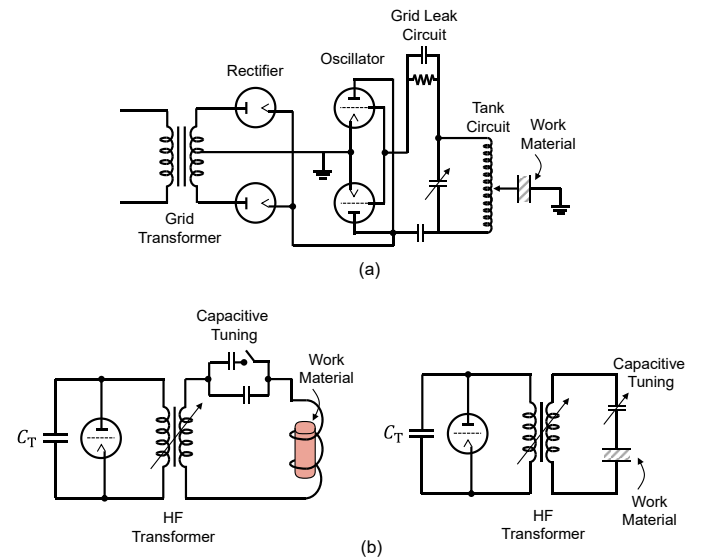

Fig. 1. (a) Schematic of directly coupled load with RF generator, (b) air-core transformer based indirectly coupled load from RF generator.

in electrification of automobiles by adopting semiconductor based electric traction system. But industrial RF heating industry is still reliant on vacuum tube technology, even though vacuum tube based RF generators offer efficiencies of only 60% [9], [10]. The industry has been satisfied with such low efficiency as an alternative solution did not exist. Advances in semiconductor technology coupled with novel resonant topologies such as Class-D, Class-E, Class-EF have led to multi-MHz DC-AC converter solutions [11]–[13]. The work in [11] is based on Class-D, which is a voltage source topology consisting of two power semiconductor switch in a half-bridge configuration. The Class-D based RF generator is operated at 13.56 MHz to cater to industrial process that require several kilowatts at one or more of the industrial, scientific and medical (ISM) band frequencies. The paper demonstrates an efficiency of 89% using silicon based IXYS RF MOSFETs. In [12], a single switch current source Class-E based RF generator is presented operating at ISM frequency of 13.56 MHz and achieves 85% efficiency. Finally in [13], a current source Class-EF topology with ISM frequency of 6.78 MHz is demonstrated. With Class-EF topology, efficiency of 91% was achieved using a low power silicon MOSFET. In these three papers, the high efficiency is achieved using soft-switching condition of zero voltage switching (ZVS). The topologies Class-D, Class-E, and Class-EF are presented in Fig. 2(a)-(c). Further advent of wide bandgap (WBG) power transistors such as gallium nitride (GaN) and silicon carbide (SiC) with improved switching capability have led a revolution in multi-MHz high efficiency DC-AC converters. Using the same ZVS soft-switching principles, however with superior WBG devices, converters operating from 2.5-13.56 MHz have shown to achieve efficiencies above 92%, which is higher than silicon MOSFET based converters. For example, SiC is predominantly preferred to operate at under 4 MHz [14]–[16]. A team from Stanford University have demonstrated both SiC (900V C3M0065090J) and GaN (650V GS66508B) based 13.56 MHz high frequency resonant converter that achieves an output efficiency of 94% [17], [18]. GaN on the other hand have proved to be far superior in operating at higher than 10 MHz and is preferred in applications like wireless power transfer (WPT) [19], [20]. The results in [17]–[19] are all based on a new current source resonant converter topology called Class-Φ_2 that operates in ZVS condition. The topology is shown in Fig. 2(d). Although the application target for [17]–[20] is towards WPT, it is important to notice that the converters are operated at one of the ISM frequency of either 6.78 MHz or 13.56 MHz.

The above overview presents that electrification of industrial heating application will have significant impact on carbon emission. However, continuing to employ inefficient vacuum tube based RF generator will lead to significant loss of energy. Therefore to increase the efficiency, industrial RF heating plants have to adopt semiconductor based RF generators. Furthermore, to maximize the return on investment it is also important to sustain the rest of existing plant with minimal modification and changes to the operation mechanism. Thus, the overall system of industrial RF heating can be considered of consisting of two components, the RF generator that
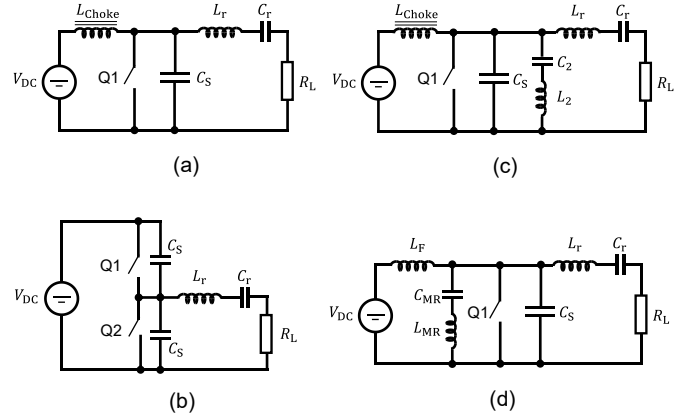

Fig. 2. Different resonant topologies that have demonstrated multi-MHz operation (a) Class-E, (b) Class-D, (c) Class-EF, and (d) Class-Φ_2.

converts DC to AC and the rest of network that forms the compensated load. The efficiency of the system thus can be shown as (1).

$$\eta_{system} = \eta_{RFGen} \cdot \eta_{Load} \tag{1}$$

Semiconductor based RF generators will require sufficient reactive energy to achieve soft-switching and ensure safe operation area (SOA) [21]. This is critical for ensuring high efficiency of the RF generator, that forms one component of (1). Therefore, the changing dynamics of work material while heating up needs to be compensated. However, a research gap exists on a comprehensive study of industrial RF heating plant load network such that the semiconductor based RF generator can be integrated as turn-key solution. There has been publications on industrial RF induction heating utilizing semiconductor technology [22], [23]. But a generalized discussion on load design does not exist. And even sparse literature is available on industrial RF dielectric heating due to higher frequency requirement. Therefore this paper takes an industrial RF dielectric heating as an example and develops a series of design equations that can be used to define current and power rating of semiconductor based RF generator. This is conducted by first developing an efficiency expression for the compensated load network which forms the second component of (1).

The remaining paper is divided into three sections. In Section II fundamental principle of dielectric heating is presented. Parallel equivalent load of dielectric work material is derived and different compensation topologies are introduced. In Section III a set of questions are posed that leads to selection of a compensation topology for industrial RF dielectric heating load structure. Analysis of the proposed load structure is discussed. A new FOM is identified that takes into consideration the load structure efficiency. Finally Section IV presents a case study and experimental validation of a small-scale prototype load.

II. Industrial RF Heating

As stated in Section I, industrial RF heating is classified between induction and dielectric heating. For induction heating

the operating frequency can be as low as 20 kHz and thus previous work have sufficiently covered its transition from vacuum tubes to semiconductor based generators [22]. On the other hand dielectric heating has not received the same attention and thus a larger knowledge gap exists in understanding dielectric loads for turn-key solutions using semiconductor based generators. Therefore in this paper the authors take industrial RF dielectric heating as an example for discussion.

A. Principle of dielectric heating

Dielectric heating is achieved by polarization of dielectric material when subjected by a time varying electric field $E(t)$. The current density $J(t)$ in the dielectric due to the electric field has been postulated by Maxwell and it comprises of conduction and displacement current as given in (2) [24],

$$J(t) = \sigma E(t) + \frac{dD(t)}{dt} \tag{2}$$

Here, σ represents the DC conductivity of the work material while $E(t)$ is the electric field applied to the work material. The second term in the equation is displacement current which originates from the polarization of the dielectric material. To provide an equivalent capacitive behavior it is better to present the time-harmonic form of the Maxwell equation given in (3) [25].

$$\nabla \times H = \sigma E + j\omega\epsilon E \tag{3}$$

ϵ is permittivity of the dielectric material. It is a complex quantity thus, breaking the dielectric permittivity of material into real and imaginary components, i.e., substituting $\epsilon = \epsilon' - j\epsilon''$ leads to (4).

$$\nabla \times H = (\sigma + \omega\epsilon'')E + j\omega\epsilon' E \tag{4}$$

Again, the second term is the displacement current. Because of imaginary component, displacement current will represent the capacitive current whereas the first part is the real load that will dissipate power in dielectric work material. Therefore the total dielectric load in (4) is a parallel combination of capacitive and resistive elements. Fig. 3 shows high frequency RF generator output applied to wood planks with an unset layer of water based glue between them. As derived earlier, the equivalent dielectric load will be a parallel combination of capacitor and resistor as shown. The values for equivalent dielectric load components are given as susceptance and conductance to maintain similarity with (4). Here A, d represent the geometrical dimensions of area, and thickness respectively, of the dielectric work material.

When RF power is applied to wood planks with a layer of unset glue between them, it induces heat and dries out the glue in a short span. The equivalent parallel capacitance and resistor values will not remain constant, which varies as the water content changes in the wood plank and the glue heats up [26], [27]. The varying load characteristics presents a significant challenge in simply replacing vacuum tube with semiconductor based RF generator. To design a suitable coupling between the semiconductor based RF generator and the
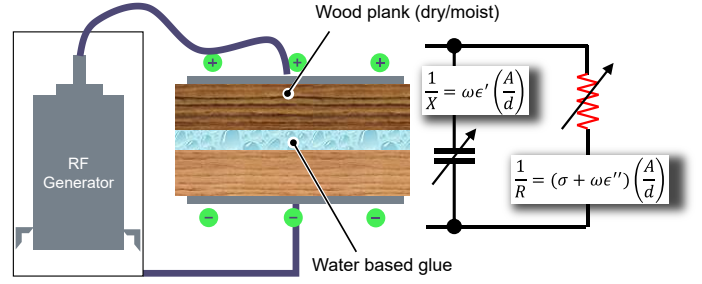

Fig. 3. Equivalent load model of dielectric work material.

existing dielectric load material, the following section covers compensation topologies.

B. Indirect coupling and compensation topologies

Majority of industrial RF dielectric heating plants over the decades have been developed with an indirectly coupled load utilizing transformer as shown in Fig. 1(b) [26]. The transformer allows for greater physical distance between the RF generator and the work material by maintaining match between generator side and load side tank circuit. The transformer can also be used for controlling power to the work material by varying its coupling [8]. Because of high voltage and high frequency operation, air-core transformers are preferred for such plants. However, the air-core leads to low coupling between the primary and secondary coils of the transformer which is compensated by series or parallel connected compensating capacitors on both sides. Similar compensating topologies are also seen in wireless power transfer applications due to relatively large distance between the transmitting and receiving coils. In WPT field four configurations of compensation topology have been identified as Series-Series (SS), Series-Parallel (SP), Parallel-Series (PS), and Parallel-Parallel (PP) as shown in Fig. 4 [28].

In Fig. 4, depending on how the capacitors are connected on the primary side of the transformer either voltage source converter (VSC) or current source converter (CSC) is utilized. This is because an inductor can be regarded as a current source and the capacitor as a voltage source. As two current sources
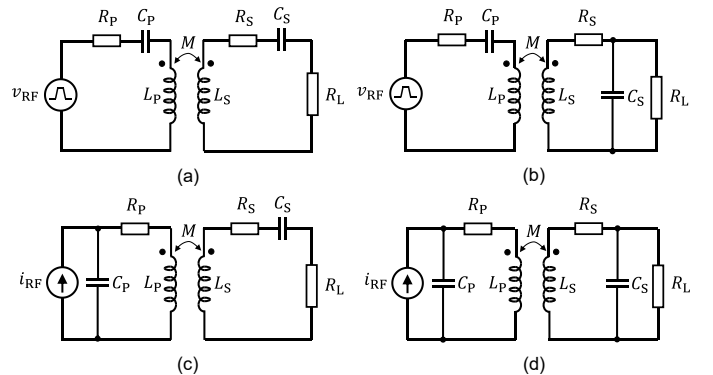

Fig. 4. Four basic compensation topologies, (a) Series-Series, (b) Series-Parallel, (c) Parallel-Series, and (d) Parallel-Parallel.

cannot be connected in series and two voltage sources cannot be placed in parallel connection, thus for series compensation network on primary a VSC is used while a CSC for parallel compensation network [29]. Furthermore on the secondary side as well, capacitors can be used in series or parallel compensation. The compensating capacitors on either side makes the load structure for industrial RF heating similar to indirectly coupled load structure with vacuum tubes presented in Fig. 1(b). In next section, arguments will be presented to choose one of these four structures for an industrial RF dielectric heating plant and additional modifications required.

III. LOAD STRUCTURE OF INDUSTRIAL RF DIELECTRIC HEATING

Previous section presents four different configurations of load structure. Therefore it is important to identify right configuration for the semiconductor based application. A few questions can be posed that can assist in deciding configuration selection, like,

1) Load dynamics has to be taken in account to maximize semiconductor device utilization in RF generator and minimize losses.
2) The RF generator is operating at several MHz (ISM band). Soft-switching for semiconductor devices shall be ensured at all load operating points.
3) The peak current in semiconductor device of RF generator shall not exceed device continuous rating under any operation point.

As shown in [28], the compensating capacitor can be designed to resonate either with leakage inductance of the coil or the coil self-inductance [30], [31]. Shown in these papers is the expression for primary side compensating capacitance (C_P) value. Table I presents the primary capacitance expression for different compensation topologies. In all four compensation configurations, the primary capacitance is dependent upon the self-inductance of primary (L_P) and secondary (L_S), as well as the secondary side compensating capacitance (C_S). But for PS and PP compensation topologies, the C_P is also dependent upon mutual inductance (M) and load resistance (R_L). As described in Section I, as the work material heats up the equivalent dielectric load characteristics changes. This is not optimal because maintaining soft-switching for the semiconductor devices is important. If the C_P value is not updated constantly with varying R_L value, the semiconductor devices can enter into hard-switching conditions which will lead to high losses and be destroyed. Therefore PS and PP topologies are eliminated from consideration.

At this stage in order to decide between SS and SP, the load impedance seen by the RF generator can be utilized. For a series compensated primary system, the load impedance will be (5),

$$Z_P = \frac{1}{j\omega C_P} + j\omega L_P + Z_r \tag{5}$$

Here Z_r is the impedance of secondary side reflected to primary side. When the secondary side tank is at resonant

Topology	Primary Capacitance (C_P)
Series-Series (SS)	$\dfrac{C_S L_S}{L_P}$
Series-Parallel (SP)	$\dfrac{C_S L_S^2}{L_P L_S - M^2}$
Parallel-Series (PS)	$\dfrac{C_S L_S}{\dfrac{M^4}{L_P C_S L_S R_L} + L_P}$
Parallel-Parallel (PP)	$\dfrac{(L_P L_S - M^2)C_S L_S^2}{\dfrac{M^4 C_S R_L}{L_S} + (L_P L_S - M^2)^2}$

frequency, the reflected load for series compensated secondary only contains the real component which is calculated as (6),

$$Z_r = R_{r(SS)} = \frac{\omega_0^2 M^2}{R_L} \tag{6}$$

and for the parallel compensated secondary the reflected resistance is calculated as (7) [31],

$$R_{r(SP)} = \frac{M^2 R_L}{L_S^2} \tag{7}$$

For dielectric loads, the resistance (R_L) are large in value usually 100 Ω or higher. Therefore series compensation on the secondary will lead to large primary current. This will lead to under utilization of semiconductor devices and the power delivered to the load cannot be maximized for the given current in RF generator. Furthermore, the equivalent dielectric load model shown in Fig. 3 consists of parallel combination of capacitor and resistor which can be utilized as parallel compensated network on secondary. Therefore for the rest of this paper the RF generator is a VSC and load topology is SP configuration. Fig. 5 shows selected SP configuration of industrial RF dielectric heating plant. Secondary side compensation capacitance is represented by equivalent dielectric load capacitance (C_L). On the secondary side there is an additional tuning inductor (L_T). The tuning inductor will match the varying dielectric load capacitance. This is how current industrial RF dielectric heating plant control power delivered to the glued wood planks. In order to maintain operation mechanism of the existing plant when replacing the vacuum tube based RF generator with semiconductor based solution this functional behavior needs to be sustained. Here the coupling between the primary and secondary coil is shown by coupling coefficient (k) as it will be used to develop an efficiency expression of the load structure.

A. Analysis of proposed load structure

The final plant model is shown in Fig. 5 with additional tuning inductor arm. To analyze the load structure and predict its behavior, Fig. 6 shows two simplifications. First, the transformer windings have been replaced by an
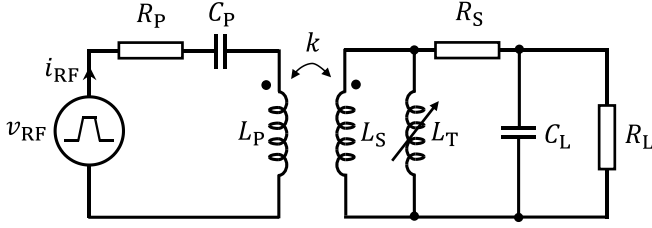
Fig. 5. Proposed Dielectric Heating Plant using semiconductor based VSC

equivalent transformer model presented in highlighted portion [32]. Second, the equivalent series resistance (ESR) of the secondary resonant tank R_S is replaced with its equivalent parallel resistance value $Q_S^2 R_S$ [33]. Here Q_S is the unloaded quality factor of secondary side resonant tank and it is defined as (8),

$$Q_S = \frac{\omega_0 (L_S // L_T)}{R_S} \quad \text{and,} \quad Q_S >> 1 \quad (8)$$
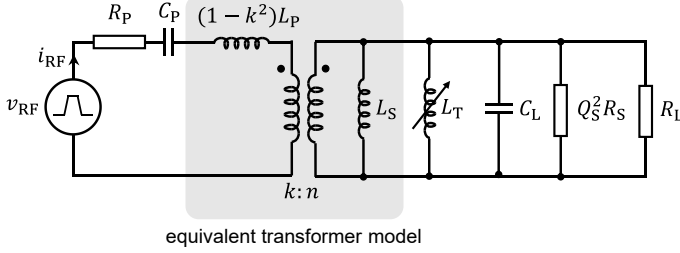

equivalent transformer model

Fig. 6. Simplified load structure with equivalent transformer model.

In Fig. 7(a) L_S and L_T are combined into a single component L_S'. By tuning L_T the combined parallel inductance L_S' can be made to resonate with C_L at the RF generator operating frequency ($f_{RF} = 1/2\pi\sqrt{L_S' C_L}$). Here R_L is combined with $Q_S^2 R_S$ and presented as R_L', as defined in (9). Finally, transferring the R_L' to primary side with turns ratio transformation gives a final simplified series resonant structure as shown in Fig. 7(b).

$$L_S' = \frac{L_S \cdot L_T}{L_S + L_T} \quad \text{and,} \quad R_L' = \frac{Q_S^2 R_S \cdot R_L}{Q_S^2 R_S + R_L} \quad (9)$$

At first the efficiency of the load structure will be evaluated. Then the expression for power dissipated in the load as well as peak current stress from the RF generator will also be derived. These three parameters help to identify three important questions, (a) output power that can be delivered to the dielectric load, (b) current rating of semiconductor devices to achieve the rated output power, (c) efficiency of the overall load under the operating conditions.

The efficiency of the load structure is defined as the ratio of power dissipated in load resistance R_L to the total power dissipated in all the resistive components. According to Fig. 7(b) the output power (P_{OUT}) is the power dissipated in $(k^2/n^2)R_L'$ and input power (P_{IN}) is total resistive power. Furthermore, since R_L' is a combination of $Q_S^2 R_S$ and the actual load resistance R_L as given in (9). It has to be taken
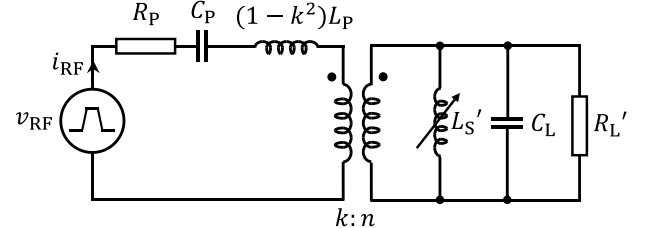
(a)
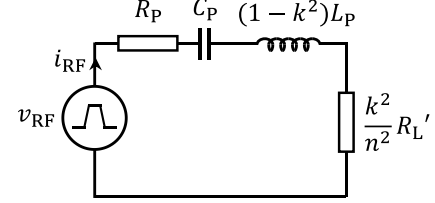
(b)

Fig. 7. (a) Load structure with combined parallel components on secondary side, and (b) simplified series resonant equivalent load seen by RF generator.

into consideration as well when calculating load structure efficiency. These two factors of load structure efficiency is given in (10) where v_{RL} is assumed to be the voltage across the secondary side components in Fig. 6.

$$\eta = \frac{P_{OUT}}{P_{IN}} = \frac{i_{RF}^2 \frac{k^2}{n^2} R_L'}{i_{RF}^2 (\frac{k^2}{n^2} R_L' + R_P)} \cdot \frac{\frac{v_{RL}^2}{R_L}}{\frac{v_{RL}^2}{\frac{R_L Q_S^2 R_S}{R_L + Q_S^2 R_S}}} \quad (10)$$

The expression in (10) is simplified and presented again as the first expression in (11). In the subsequent steps in (11) the resistances are replaced with quality factors whose definitions are provided together, underneath the expression. As the efficiency of a resonating inductive link depends on many parameters, such as the ESR of windings, value of inductance, coupling coefficient etc. Discussing the impact of each term explicitly on the overall efficiency can get convoluted as the parameters are all interlinked. Utilizing quality factor to assess efficiency of high frequency structures is often preferred. But as shown in the efficiency expression (11) both loaded and unloaded quality factors are involved. Therefore in the final efficiency expression two new terms are defined,

$$FOM = k\sqrt{Q_{SL} Q_P} \quad \text{and,} \quad \alpha = \frac{L_S}{L_T} \quad (12)$$

$k\sqrt{Q_{SL} Q_P}$ is defined as figure of merit (FOM) that ties together unloaded and loaded quality factor of both primary and secondary side. Similar FOM have also been defined for WPT load structures [34]. The FOM also contains the coupling coefficient k between the two coils of the transformer. The FOM can be imagined as a quantitative study of the construction of the RF dielectric load. The second term defined in the efficiency expression (11) is tuning ratio (α). When

$$\eta = \frac{\frac{k^2}{n^2}R'_L}{\frac{k^2}{n^2}R'_L + R_P} \cdot \frac{Q_S^2 R_S}{Q_S^2 R_S + R_L} = \frac{\frac{k^2}{n^2} \cdot \frac{L'_S Q_S Q_L}{Q_S + Q_L}}{\frac{L_P}{Q_P} + \frac{k^2}{n^2} \cdot \frac{L'_S Q_S Q_L}{Q_S + Q_L}} \cdot \frac{Q_S}{Q_S + Q_L} = \frac{\frac{k^2 L_T Q_S Q_L Q_P}{(L_S + L_T)(Q_S + Q_L)}}{1 + \frac{k^2 L_T Q_S Q_L Q_P}{(L_S + L_T)(Q_S + Q_L)}} \cdot \frac{Q_S}{Q_S + Q_L}$$

$$\eta = \frac{k^2 Q_{SL} Q_P}{(1 + \alpha) + k^2 Q_{SL} Q_P} \cdot \frac{Q_{SL}}{Q_L} = \frac{(k\sqrt{Q_{SL} Q_P})^2}{(1 + \alpha) + (k\sqrt{Q_{SL} Q_P})^2} \cdot \frac{Q_{SL}}{Q_L} = \frac{FOM^2}{(1 + \alpha) + FOM^2} \cdot \frac{Q_{SL}}{Q_L} \qquad (11)$$

$$Q_S = \frac{\omega_0 L'_S}{R_S}, \qquad Q_L = \frac{R_L}{\omega_0 L'_S}, \qquad Q_P = \frac{\omega_0 L_P}{R_P}, \qquad Q_{SL} = \frac{Q_S Q_L}{Q_S + Q_L}, \qquad Q_{L2} = \sqrt{\frac{(1 - k^2)L_P}{C_P}} \cdot \frac{1}{R}, \qquad R = R_P + \frac{k^2}{n^2}R'_L$$

L_T varies to match C_L, the efficiency of the load structure is impacted as the value of α changes.

Finally, based on the simplified series resonant equivalent load seen by the RF generator as shown in Fig. 7(b) the peak value of output current from the RF generator can be estimated as (13) [35]. And using (11), (13) the output power dissipated in R_L is calculated, given in (14). V_{DC} in the expression is DC link voltage applied to the RF generator. The AC output from RF generator oscillates between $\pm V_{DC}$.

$$i_{RF(p)} = \frac{4V_{DC}}{\pi R \sqrt{1 + (Q_{L2}(\frac{\omega}{\omega_0} - \frac{\omega_0}{\omega}))^2}} \qquad (13)$$

$$P_{OUT} = \eta \frac{i_{RF(p)}^2}{2} R = \eta \frac{8V_{DC}^2}{\pi^2 R(1 + (Q_{L2}(\frac{\omega}{\omega_0} - \frac{\omega_0}{\omega}))^2)} \qquad (14)$$

The discussion so far provides three sets of expressions to estimate the efficiency of industrial RF dielectric load design, the peak RF generator current and the output power dissipated in the load. Fig. 8 is a contour plot for the three quantities. The DC link voltage (V_{DC}) defined for the plot is 5 kV, resulting in 10 kV peak-peak AC output from RF generator at 13.56 MHz. To understand the impact of different size of the transformer coils, the self inductance is varied from $0.5\rightarrow5$ μH at unity turns ratio of the coils. The primary coil ESR (R_P) is fixed at 0.5 Ω and secondary coil ESR (R_S) at 0.1 Ω. The discussion on selecting these ESR values is provided in next subsection. The coupling coefficient is set at 0.55 which is typical for concentric helical winding type design with air-core. The load resistor (R_L) is set at 100 Ω. The tuning inductor (L_T) is set at 0.5 μH that varies the tuning ratio (α) from $1\rightarrow10$.

Fig. 8(a) shows the efficiency of the load design. It can be seen that higher FOM leads to higher efficiency in the load. However the efficiency is not linearly progressing as the FOM increases. For example, in Fig. 8(b) as the RF generator peak current value increases from 80 to 100 A, the output power increases from 100 to 150 kW in Fig. 8(c). But the highest efficiency of 98% is only achieved when FOM is beyond 18 and drops linearly as tuning ratio (α) increases from 1 to 8. This is because as transformer coils size increases from $0.5\rightarrow5$ μH, the primary quality factor (Q_P) increases linearly with it. However the secondary quality factor (Q_S) growth slows down because of parallel tuning inductor arm (L_T). This, along with decreasing loaded secondary quality factor (Q_L) leads to the efficiency pattern achieved in Fig. 8(a). As stated in

Section I, that the dynamics of work material changes as it heats up, i.e., R_L varies over time as RF power is applied. This will lead to change in output power (P_{OUT}) which in turn will impact output current (i_{RF}) from the RF generator. As shown in [21], [36], this can lead to hard-switching or partial hard-switching. However showcasing the impact of individual parameters like R_L, L_T, and k separately in this paper will be difficult. Therefore the unifying quantity - FOM, that ties together all of these individual parameters is presented. And one is free to vary any of these individual parameters to see the impact on converter dynamics.

The values taken here for the contour plot are reasonable estimates based on the literature survey, and are only intended to showcase the capability of the discussion thus far in designing an industrial RF dielectric load structure.

B. Discussion on FEA based ESR estimation

The values for the winding inductance, their ESR values, and coupling coefficient are important as they form the constituents of FOM. Amongst the various components of load, the transformer has the maximum number of degrees of freedom in terms of physical design which will impact the FOM and therefore the efficiency. Various architectures of the transformer are feasible. In industrial RF heating applications copper tube based helical structures are preferred [8]. Liquid cooling is usually employed given the high power requirement of RF heating plants. The hollow structure of the cooper tubes thus present an opportunity to effectively dissipate heat without additional cooling systems. Utilizing the hollow structure for flowing cooling liquid also does not impact electrical performance of the system since the RF frequency forces the current on the circumference due to skin effect.

Amongst the different parameters, the copper tube ESR plays a significant role in deciding efficiency of the load network. To estimate reasonable values of ESR for the primary and secondary side coil, finite element analysis (FEA) is conducted using COMSOL Multiphysics simulation on 2D axio-symmetric geometry of helical design of the transformer where secondary coil sits within the primary coil. The 2D axio-symmetric structure of the transformer is shown in Fig. 9.

Previous works have calculated coil ESR using analytical method dependent upon skin effect at specific frequencies [37]. But it does not consider extremely large impedance near self
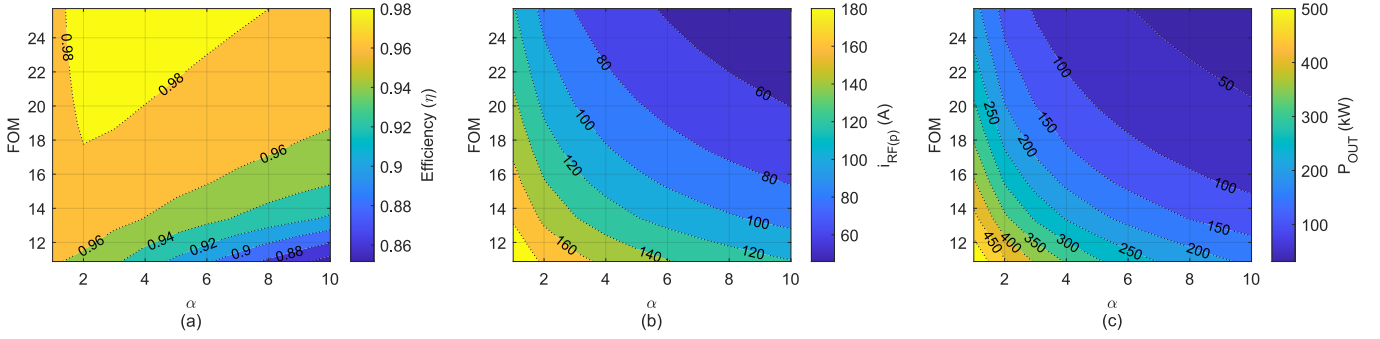
Fig. 8. Variation of load parameters for varying self-inductance value of inductive power link from 0.5→5 μH, (a) efficiency, (b) output power, and (c) peak current in primary side.
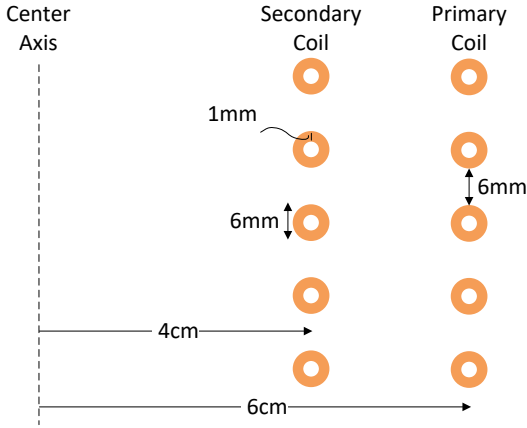

Fig. 9. 2D Axio-symmetric model of the transformer in COMSOL Multiphysics simulation with 5 turns each on Primary and Secondary Coil.

resonant frequency when the inductive and capacitive effect cancel each other out [38]. Therefore COMSOL Multiphysics based FEA is conducted to estimate the ESR values. The ESR values for both primary and secondary coil is extracted at multiple frequencies as shown in Fig. 10. Furthermore the ESR value changes with number of turns, therefore number of turns is swept as indicated, starting from 5 to 11 turns. At 5 turns the coils have lowest ESR values which increases as the number of turns increases and maximum for 11 turn coil. Solid lines in Fig. 10 indicate primary coil ESR whereas the dashed lines are for secondary coil. Given that secondary coil helix is designed within primary coil as shown in Fig. 9, for the same number of turns the total length of secondary coil will be smaller than primary coil and thus the ESR value is lower for secondary coil as compared to primary coil. Fig. 10(a) represents ESR values for the transformer dimensions specified in Fig. 9. All the dimensions indicated in Fig. 9 are then increased by a factor of 2 and then by factor of 4 and presented as Dimension $2x$ and $4x$ in Fig. 10(b), and (c) respectively.

Fig. 10 shows that as the dimension of the transformer increases from $x \rightarrow 2x \rightarrow 4x$, the ESR at 1 MHz decreases due to increasing copper tube thickness. However the self resonant frequency of the coils also drops. For example in Dimension x the resonant frequency of primary coil at 11 turns

is 15 MHz which drops down to 4 MHz in Dimension $4x$. This will limit the operating frequency of the system. Therefore for the contour plot in Fig. 8 primary coil ESR (R_P) is selected at 0.5 Ω (marked by star in Fig. 10(a)) and secondary coil ESR (R_S) at 0.1 Ω which are worst case values at 13.56 MHz.

IV. CASE STUDY

The FEA model developed to analyse the coil ESR has been extended to design a transformer for a case study. The transformer is designed with 11 turns on the primary coil for higher impedance and limit the current from the RF generator. The secondary coil is designed with 5 turns. The winding dimensions are same as Fig. 9. The primary coil diameter is 12 cm while the secondary is 8 cm in diameter. The transformer and overall series-parallel (SP) load configuration is shown in Fig. 11. In the load structure analysis in Section III a tuning inductor L_T is added to compensate the varying dielectric load capacitance C_L. But for the case study a fixed capacitance is used as the dielectric load C_L shown in Fig. 11(b). Therefore no tuning inductor is required to maintain load behavior during operation. Both the C_L and C_P are vacuum type capacitors, that can sustain high current and high voltage at MHz frequency with extremely low inductance value of less than 9 nH. This load is also presented in [39].

The designed transformer is tested using an LCR meter for the inductance values of the primary and secondary coil as well as the mutual inductance between the two sides. The results are presented in Fig. 12. The primary coil self inductance (L_P) stays constant at 9 μH until 10 MHz. The secondary coil has self inductance (L_S) value of 2.4 μH until 20 MHz. Using the mutual inductance (M) value of 2.46 μH from Fig. 12(b) the coupling coefficient ($k = M/\sqrt{L_P L_S}$) is calculated to be 0.53 at 6.76 MHz. The measured results are also compared with simulation values from COMSOL Multiphysics. As results show the simulation has been successful in predicting the inductance values as well as the self-resonant frequency of the windings. The first resonant point occurs beyond 20 MHz, therefore the transformer is operable until 13.56 MHz.

In Section I various resonant converter topologies have been presented that have shown multi-MHz operation capability. However single-switch topoligies shown in Fig. 2, that are preferred for high frequency operation suffer from low power
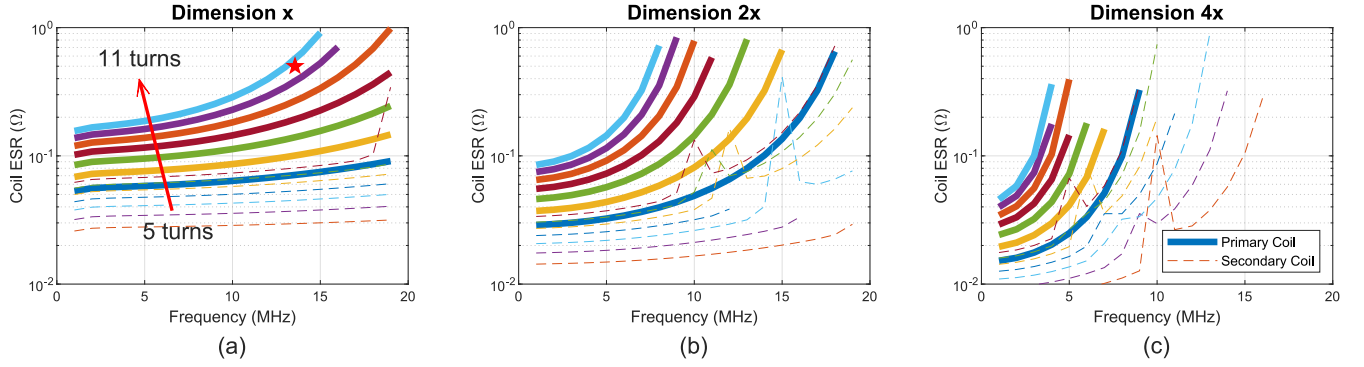
Fig. 10. Variation of ESR in primary (solid) and secondary (dashed) coil with increasing number of turns in, (a) Dimension x, (b) Dimension 2x, and (c) Dimension 4x.
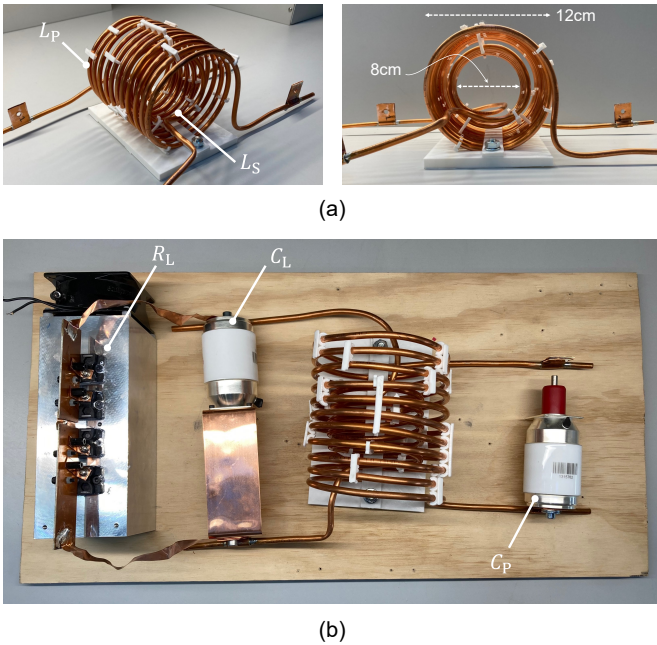

Fig. 11. (a) Designed transformer with 11 turns on primary and 5 turns on secondary, (b) Series-Parallel load configuration with the designed transformer [39].
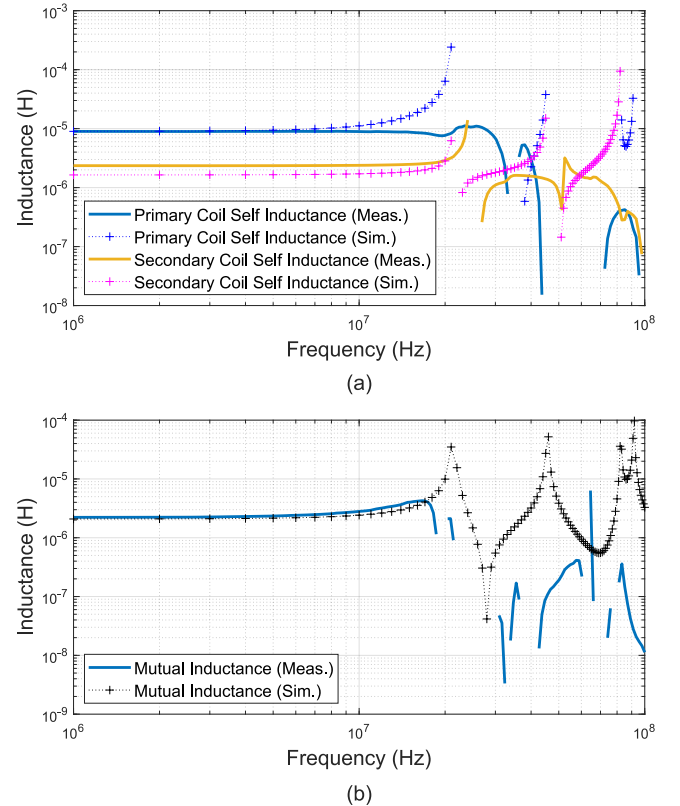

Fig. 12. (a) Self inductance of the primary and secondary side and, (b) Mutual inductance between the winding of the inductive power linke using FEM simulation (COMSOL) and measurement from RLC meter.

handling capability which indicates low semiconductor device utilization as presented in [39]. Also shown in the same paper, four-switch topologies have a higher power handling capability. Therefore in this work a four-switch topology called Class-PN is utilized for the RF generator. Similar to full-bridge (FB), Class-PN is also a voltage source type converter however unlike FB where the load is floating Class-PN allows for grounding the load [39]. The schematic of the Class-PN is presented in Fig. 13(a). It shows two half-bridge structures that are connected at the switching node. The coupled inductors L_1 and L_2 ensures the voltage across capacitor C is equal to V_{DC}. The load shown in the schematic is a simplified series resonant structure for representation purposes. As discussed in Section I that for high frequency operation GaN devices have been preferred. The four switches in Class-PN are GaN devices (GS66506T) from Gansystems rated at 650 V and 22

A. The device is chosen due to its low output capacitance (C_{OSS}) of 49 pF at 400 V. Furthermore in Fig. 13(b) the PCB layout for the four GaN devices of Class-PN topology is shown. The switching node is kept non-overlapping to the drain terminal of $Q1, Q3$ and source terminal of $Q2$, and $Q4$ thus minimizing the parasitic capacitance. Also, the layout is designed symmetrically such that the GaN devices are kept in close proximity to reduce parasitic inductances.

The load presented in Fig. 11 is connected to Class-PN RF generator operating at 6.76 MHz. The primary side compensating capacitor (C_P) and the load capacitance (C_L) is
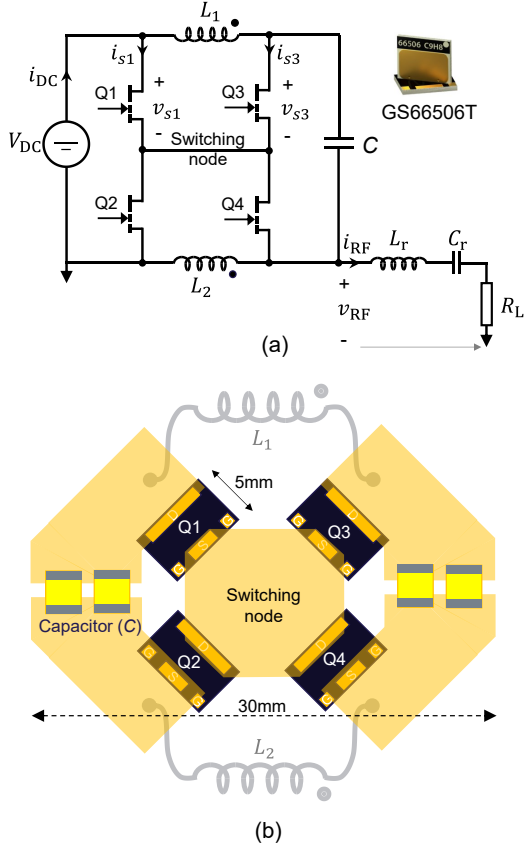
Fig. 13. Four-switch ressonant topology called Class-PN and the GaN device used (GS66506T) [39], (b) PCB layout for the four GaN devices in Class-PN topology.

Fig. 14. Comparison between experimental measurement and model prediction.

set such that the simplified series resonant equivalent load seen by the Class-PN RF generator has natural frequency (f_0) of 6.5 MHz. This ensures that the RF generator operates in inductive region and maintains soft-switching. As the DC link voltage (V_{DC}) is increased the Class-PN RF generator input current (i_{DC}) and output current (i_{RF}) are measured using current probe CP030 [40]. The load resistance (R_L) is 33 Ω. The output voltage on load resistance is also measured which gives the output power dissipated in the load (P_{OUT}). The output voltage is measured using differential probe HVD3605A [41]. Fig. 14 plots peak i_{RF} and P_{OUT}. As V_{DC} increases from 100 to 300 V, the P_{OUT} is increasing from 56 to 750 W respectively. Dashed lines in the Fig. 14 represents the predicted values from the model developed in (11) - (14). For the model the secondary coil self inductance is taken as 3.1 μH, which is higher than 2.4 μH as measured in Fig. 12. The additional 0.7 μH parasitic inductance coming from connecting foils and terminals. The coupling coefficient is set at 0.5 in the model which is slightly lower than 0.53 measured. This can also be explained by additional parasitic inductance due to connecting foils on both the primary and the secondary side that reduce the overall coupling between the winding. The experimental measurement is in close agreement with the model predicted values. The FOM is calculated to be 7.7 for this load structure. The value of Q_L is 0.2506, and Q_{SL} being a parallel combination of
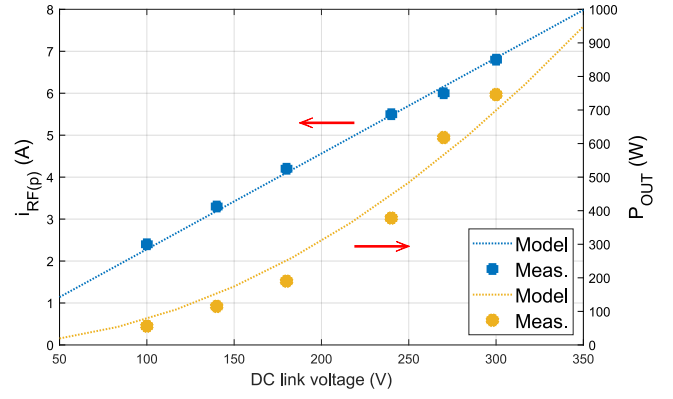
Q_L and Q_S is also equal to 0.2506. Using these values, the model predicts 98.3% efficiency for the load structure in this case study. The efficiency is comparable to the study done in Sec. III-A even though FOM is relatively lower. That is due to the absence of tuning inductor (L_T) in the load structure of case study as it makes the tuning ratio (α) equal to 0 in the efficiency calculation in (11). Fig. 15 shows experimental waveform at 300 V DC link voltage. It shows the RF generator input current (i_{DC}), output current (i_{RF}) and output voltage (v_{RF}) as well as load resistance voltage (v_{R_L}). As discussed for Fig. 13(b) that focus had been on symmetrical layout, compact design and reducing parasitic capacitance to minimize EMI issues. Shown in 15(a) the RF generator output voltage (v_{RF}). The rising and falling edges will correspond to the drain-source voltage of the devices $Q1 \rightarrow Q4$. For example, when $Q1$ and $Q4$ turns-on a positive voltage rise is seen in v_{RF}. This will be same as the rising voltage across the drain-source of $Q2$ and $Q3$. Similarly vice-versa for the falling edge of v_{RF}. For the 750 W output power the i_{DC} is measured to be 2.8 A which gives an input DC power of 840 W and the overall system efficiency including the RF generator and load is approximately 90%.

V. CONCLUSION

This paper has addressed the knowledge gap that exists in understanding industrial RF heating load structure when transitioning from vacuum tubes to semiconductor based VSC topologies. The knowledge gap has been a major hurdle towards retrofitting existing industrial plants with semiconductor based turn-key solution and replace inefficient vacuum tube based RF generator that are only 60% efficient. The paper identifies series-parallel load configuration for industrial RF dielectric heating plants when powered with semiconductor based VSC topologies. The load structure behaviour can be estimated by model expression which can be used for deciding specification of different components in the load and RF generator. An air-core transformer is designed using FEA that successfully estimates coils ESR and coupling coefficient. A new FOM is identified that quantifies the construction of the load structure based on loaded and unloaded quality factors.
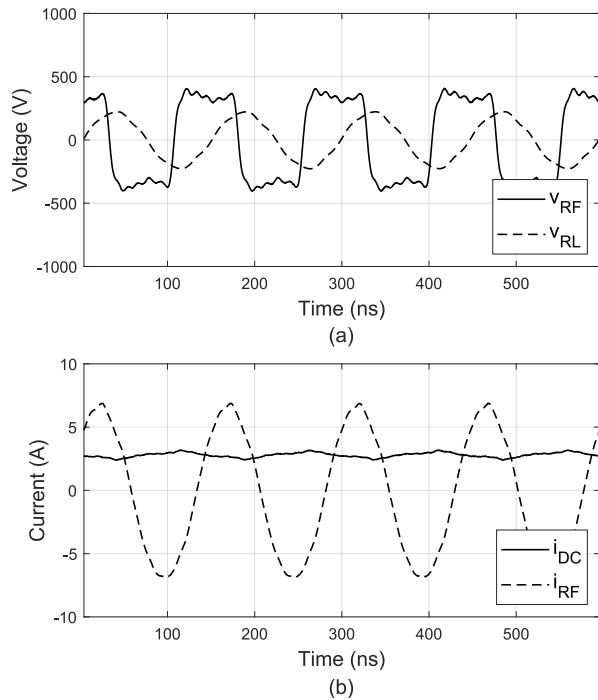
Fig. 15. Experimental waveform for 300 V DC link voltage and f_{SW} of 6.76 MHz.

Finally a case study shows that a small-scale prototype can achieve efficiency close to 90% at 6.76 MHz frequency for output power of 750 W.

ACKNOWLEDGMENT

REFERENCES

[1] A. Hasanbeigi, L. A. Kirshbaum, B. Collison, and D. Gardiner, "Electrifying U.S. Industry: A Technology- and Process-Based Approach to Decarbonization," *Renewable Thermal Collaborative*, 2021.

[2] K. Pinder, "Induction and dielectric heating," *Electrical Engineering*, vol. 66, no. 2, pp. 149–160, 1947.

[3] F. M. Clark and M. E. Scoville, "Capacitors for High-Frequency Induction-Heating Circuits," *Transactions of the American Institute of Electrical Engineers*, vol. 64, no. 11, pp. 791–796, 1945.

[4] R. Bierwirth and C. Hoyler, "Radio-Frequency Heating Applied to Wood Gluing," *Proceedings of the IRE*, vol. 31, no. 10, pp. 529–537, 1943.

[5] M. J. Maiers, "A survey of dielectric heating," *Electrical Engineering*, vol. 64, no. 6, pp. 210–211, 1945.

[6] W. Roberds, "The Use of Radio Frequencies to Obtain High-Power Concentrations for Industrial-Heating Applications," *Proceedings of the IRE*, vol. 33, no. 1, pp. 9–14, 1945.

[7] G. W. Scott, "Induction and Dielectric Heating," *Transactions of the American Institute of Electrical Engineers*, vol. 67, no. 2, pp. 885–892, 1948.

[8] H. Dittrich, *Tubes for R.F. Heating*, 1971.

[9] T. Koral, "Radio Frequency Heating and Post-Baking - A maturing Technology that can still offer significant benefits," *Biscuit World*, vol. 7, no. 4, 2004.

[10] T. L. Wilson, "Radio-Frequency Dielectric Heating in Industry," *Electric Power Research Institute, California, USA*, 3 1987.

[11] "3kW and 5kW half-bridge Class-D RF generators at 13.56MHz and 89% efficiency and limited frequency agility," *IXYS Corporation*, 2002.

[12] "PRF-1150 1kW 13.56MHz Class E RF Generator Evaluation Module," *IXYS Corporation*, 2019.

[13] S. Aldhaher, D. C. Yates, and P. D. Mitcheson, "Modeling and Analysis of Class EF and Class E/F Inverters With Series-Tuned Resonant Networks," *IEEE Transactions on Power Electronics*, vol. 31, no. 5, pp. 3415–3430, 2016.

[14] A. B. Jorgensen, U. R. Nair, S. Munk-Nielsena, and C. Uhrenfeldt, "A SiC MOSFET Power Module With Integrated Gate Drive for 2.5 MHz Class E Resonant Converters," in *CIPS 2018; 10th International Conference on Integrated Power Electronics Systems*, 2018, pp. 1–6.

[15] F. Denk, K. Haehre, C. Simon, S. Eizaguirre, M. Heidinger, R. Kling, and W. Heering, "25 kW High Power Resonant Inverter Operating at 2.5 MHz based on SiC SMD phase-leg modules," in *PCIM Europe 2018; International Exhibition and Conference for Power Electronics, Intelligent Motion, Renewable Energy and Energy Management*, 2018, pp. 1–7.

[16] S. Guo, L. Zhang, Y. Lei, X. Li, F. Xue, W. Yu, and A. Q. Huang, "3.38 Mhz operation of 1.2kV SiC MOSFET with integrated ultra-fast gate drive," in *2015 IEEE 3rd Workshop on Wide Bandgap Power Devices and Applications (WiPDA)*, 2015, pp. 390–395.

[17] J. Choi, D. Tsukiyama, and J. Rivas, "Evaluation of a 900 V SiC MOSFET in a 13.56 MHz 2 kW resonant inverter for wireless power transfer," in *2016 IEEE 17th Workshop on Control and Modeling for Power Electronics (COMPEL)*, 2016, pp. 1–6.

[18] J. Choi, D. Tsukiyama, Y. Tsuruda, and J. Rivas, "13.56 MHz 1.3 kW resonant converter with GaN FET for wireless power transfer," in *2015 IEEE Wireless Power Transfer Conference (WPTC)*, 2015, pp. 1–4.

[19] L. Gu and J. Rivas-Davila, "1.7 kW 6.78 MHz Wireless Power Transfer with Air-Core Coils at 95.7% DC-DC Efficiency," in *2021 IEEE Wireless Power Transfer Conference (WPTC)*, 2021, pp. 1–4.

[20] J. M. Arteaga, S. Aldhaher, G. Kkelis, D. C. Yates, and P. D. Mitcheson, "Multi-MHz IPT Systems for Variable Coupling," *IEEE Transactions on Power Electronics*, vol. 33, no. 9, pp. 7744–7758, 2018.

[21] O. Knecht, R. Bosshard, and J. W. Kolar, "High-Efficiency Transcutaneous Energy Transfer for Implantable Mechanical Heart Support Systems," *IEEE Transactions on Power Electronics*, vol. 30, no. 11, pp. 6221–6236, 2015.

[22] O. Lucía, P. Maussion, E. J. Dede, and J. M. Burdío, "Induction Heating Technology and Its Applications: Past Developments, Current Technology, and Future Challenges," *IEEE Transactions on Industrial Electronics*, vol. 61, no. 5, pp. 2509–2520, 2014.

[23] T. S. Aunsborg, S. B. Duun, S. Munk-Nielsen, and C. Uhrenfeldt, "Development of a Current Source Resonant Inverter for High Current MHz Induction Heating," *IET power electronics*, vol. 15, no. 1, p. 1–10, 2022.

[24] E. Kuffel, W. S. Zaengl, and J. Kuffel, "Non-destructive insulation test techniques," *High Voltage Engineering*, vol. 2nd Edition Butterworth-Heinemann Publication.

[25] M. S. Ferdous, "Design of a Radio Frequency Heating System for Electrolytic Liquids and Sludges," *Master Thesis, The University of British Columbia*, 2015.

[26] J. Tomljenovic, "200 kW High Frequency Press for Dielectric Heating," *Plustherm Point GmbH Seminarstrasse 102, 5430 Wettingen, Switzerland*.

[27] S. Wang, "On the relationship between dielectric dissipation-factor and angular frequency," in *[1991] Proceedings of the 3rd International Conference on Properties and Applications of Dielectric Materials*, 1991, pp. 1080–1082 vol.2.

[28] S. Li and C. C. Mi, "Wireless Power Transfer for Electric Vehicle Applications," *IEEE Journal of Emerging and Selected Topics in Power Electronics*, vol. 3, no. 1, pp. 4–17, 2015.

[29] Y. Zhang, Z. Yan, T. Kan, X. Zeng, S. Chen, and C. C. Mi, "Modeling and Analysis of a Strongly Coupled Series–Parallel-Compensated Wireless Power Transfer System," *IEEE Journal of Emerging and Selected Topics in Power Electronics*, vol. 7, no. 2, pp. 1364–1370, 2019.

[30] A. J. Moradewicz and M. P. Kazmierkowski, "Contactless Energy Transfer System With FPGA-Controlled Resonant Converter," *IEEE Transactions on Industrial Electronics*, vol. 57, no. 9, pp. 3181–3190, 2010.

[31] C.-S. Wang, O. Stielau, and G. Covic, "Design Considerations for a Contactless Electric Vehicle Battery Charger," *IEEE Transactions on Industrial Electronics*, vol. 52, no. 5, pp. 1308–1314, 2005.

[32] K. V. Schuylenbergh and R. Puers, *Inductive Powering - Basic Theory and Application to Biomedical Systems*, 2009.

[33] R. R. Harrison, "Designing Efficient Inductive Power Links for Implantable Devices," *2007 IEEE International Symposium on Circuits and Systems*, pp. 2080–2083, 2007.

[34] R. Bosshard, J. W. Kolar, J. Mühlethaler, I. Stevanović, B. Wunsch, and F. Canales, "Modeling and η - α -Pareto Optimization of Inductive Power Transfer Coils for Electric Vehicles," *IEEE Journal of Emerging and Selected Topics in Power Electronics*, vol. 3, no. 1, pp. 50–64, 2015.

[35] M. K. Kazimierczuk and D. Czarkowski, *Resonant Power Converters*, 2nd ed., 2010.

[36] M. Kasper, R. M. Burkart, G. Deboy, and J. W. Kolar, "ZVS of Power MOSFETs Revisited," *IEEE Transactions on Power Electronics*, vol. 31, no. 12, pp. 8063–8067, 2016.

[37] M. Pinuela, D. C. Yates, S. yszyn, and P. D. Mitcheson, "Maximizing DC-to-Load Efficiency for Inductive Power Transfer," *IEEE Transactions on Power Electronics*, vol. 28, no. 5, pp. 2437–2447, 2013.

[38] COMSOL Multiphysics, "Axisymmetric Approximation of 3D Inductor," https://www.comsol.com/model/download/891031/models.acdc.axisymmetric_approximation_of_inductor_3d.pdf, [Online; accessed June 2022].

[39] F. Ahmad, A. B. Jørgensen, and S. Munk-Nielsen, "Four-switch Class-PN Power Amplifier for High Power Handling Capability in Wireless Power Transfer," in *2022 International Power Electronics Conference (IPEC-Himeji 2022- ECCE Asia)*, 2022, pp. 968–972.

[40] Teledyne Lecroy, "Current Probes," https://cdn.teledynelecroy.com/files/pdf/current-probes-datasheet.pdf, 2022, [Online; accessed June 2022].

[41] ——, "High Voltage Differential Probes," https://cdn.teledynelecroy.com/files/pdf/hvd3000a-probes-datasheet.pdf, 2022, [Online; accessed June 2022].

Faheem Ahmad Faheem Ahmad received the B.Sc. degree in Electrical Engineering from Delhi Technological University, Delhi India in 2014 and M.Sc. degree in Energy Engineering with a specialization in power electronics and drives from Aalborg University, Aalborg, Denmark, in 2020.

He is currently a Research Assistant and pursuing PhD at AAU Energy, Aalborg University. He previously worked with Toshiba Semiconductors as Systems Engineer on residential solar inverters between 2015-2018. His research interests include high frequency converter topology, resonant converters, and wide bandgap power semiconductors.

Asger Bjørn Jørgensen Asger Bjørn Jørgensen received the M.Sc. degree in energy engineering with a specialization in power electronics and the Ph.D. degree from Aalborg University, Aalborg, Denmark, in 2016 and 2019, respectively.

He is currently a Assistant Professor at AAU Energy, Aalborg University. His research interests include power module packaging, wide bandgap power semiconductors, and multiphysics finite element analysis.

Stig Munk-Nielsen Stig Munk-Nielsen (Member, IEEE) received the M.Sc. and Ph.D. degrees from Aalborg University, Aalborg, Denmark, in 1991 and 1997, respectively.

He is currently a Professor at AAU Energy, Aalborg University. His research interests include LV and MV Si, SiC, and GaN converters, packaging of power electronic devices, electrical monitoring apparatus for IGBTs, failure modes, and device test systems. In the last ten years, he has been involved in or has managed ten research projects and has authored or coauthored 242 international power electronic papers.